Article

Atomic Layer Deposition of Pt on the Surface Deactivated by Fluorocarbon Implantation: Investigation of the Growth Mechanism

Woo-Hee Kim,[#] Kihyun Shin,[#] Bonggeun Shong, Ludovic Godet, and Stacey F. Bent*
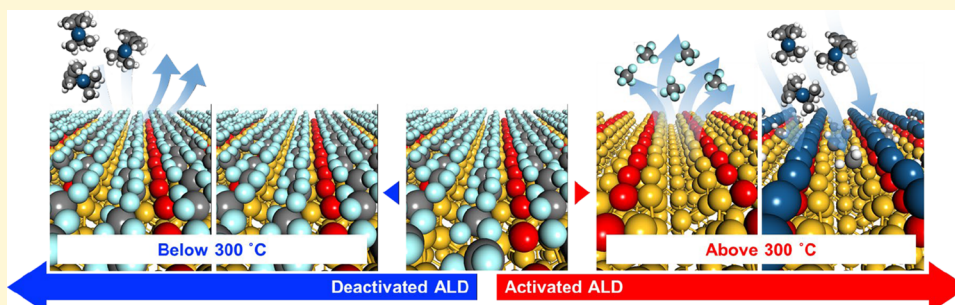
Read Online

ACCESS | Metrics & More | Article Recommendations | SI Supporting Information

ABSTRACT: Selective atomic layer deposition (ALD) using surface-controlled reactivity is attracting a great deal of attention as a simple bottom-up patterning process that can provide both continued dimensional scaling and accurate pattern placement for next-generation nanoelectronics. We previously reported topographically selective deposition through Pt ALD using a MeCpPtMe$_3$ precursor and an O$_2$ counter reactant on fluorocarbon (CF$_x$)-modified surfaces; however, gradual loss of selectivity in the CF$_x$-modified regions was observed during the Pt ALD process. This work develops a fundamental understanding of the microscopic growth mechanisms of Pt ALD on the CF$_x$-modified surface using a combination of experimental analyses and theoretical methods. The Pt growth characteristics on the CF$_x$ surface are investigated within a temperature window from 225 to 350 °C, and the results show a sharp sensitivity to growth temperature, with significant Pt growth occurring at temperatures above 300 °C. Through density functional theory (DFT) calculations, the reaction energies for adsorption of oxygen and the MeCpPtMe$_3$ precursor as well as formation of reaction products of CF$_x$ degradation are determined. Based on experimental results in conjunction with the DFT calculations, we show that while lower temperature Pt ALD (<300 °C) on CF$_x$-modified surfaces can be significantly retarded because of a lack of MeCpPtMe$_3$ chemisorption, the surface reaction pathways for Pt ALD on CF$_x$-modified surfaces at temperatures above 300 °C can proceed through oxygen adsorption and CF$_4$ desorption followed by Pt nucleation in CF$_x$-degraded regions.

INTRODUCTION

Directing atoms to a specific location in a desired growth area, called bottom-up fabrication, is a long sought-after goal in nanotechnology; this approach can advance a variety of practical applications such as catalysis,[1−4] sensing,[5] and energy harvesting[6] as well as semiconductor processing with three-dimensional (3-D) architectures.[7−9] In this context, area-selective atomic layer deposition (AS-ALD) has recently emerged as one of the potential solutions in which self-aligned thin film patterns can be placed directly on a predetermined area in a selective manner by making use of inherent surface chemistry in ALD.[8−11] Thereby, the number of conventional photolithography and etching steps is expected to be drastically reduced. For this reason, a significant effort is currently underway in both industry and academia to develop robust and reliable AS-ALD methods.[12] The predetermined growth area can be defined by attaching surface-inhibitory molecules, and the use of self-assembled monolayers (SAMs) has been the most popular choice for deactivating unwanted growth in the majority of previous studies on AS-ALD.[13−18] However, the

SAM method possesses some challenges. For example, in one study, inherent selectivity loss was found in the edge regions of 3-D geometries with high curvature because of the presence of steric hindrance between bulky SAM molecules, suggesting difficulty in inhibiting growth against ALD processes in 3-D nanostructures with sub-100 nm feature sizes.[19]

Alternative methods for inhibition of ALD are being pioneered, including adoption of small inhibitor molecules,[8] plasma treatment,[7] and ion implantation[9] to deactivate the unwanted nongrowth area. Indeed, in our recent work that uses a hydrophobic CF$_x$-implanted layer for AS-ALD (see the schematic proof of concept shown in Figure S1), we
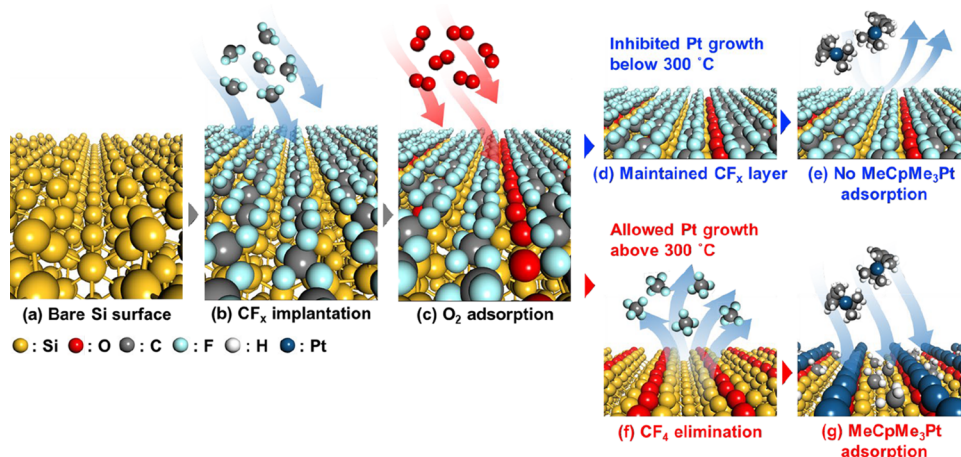
Figure 1. Schematic representation of the reaction mechanisms during Pt ALD on a CF_x surface. (a, b) First, CF_x implantation on the Si surface is carried out. (c) Next step is Pt ALD with sequential O_2 and $MeCpPtMe_3$ pulses. At the start of the O_2 half-reaction, an O-covered surface is generated beneath the CF_x layer. (d, e) During the $MeCpPtMe_3$ half-reaction, the CF_x layer is thermally stable at a substrate temperature below 300 °C, so the $MeCpPtMe_3$ adsorption is inhibited. (f, g) However, the CF_x layer becomes degraded at a substrate temperature above 300 °C, liberating volatile CF_4 species, and hence adsorption of incoming $MeCpPtMe_3$ is possible, eventually leading to Pt nucleation and growth.

successfully demonstrated topographical selectivity in which thin film growth only on vertical sidewalls of 3-D patterned Si fin structures was achieved.[9] Nevertheless, a gradual loss of selectivity seems inevitable with an increasing number of ALD cycles. In reality, almost all the AS-ALD studies regardless of surface-deactivation materials have consistently revealed selectivity loss during ALD.[11,18−21] In other words, the character of the inhibited nongrowth area is altered when exposed to the subsequent ALD process that uses alternating exposure of precursor and counter reactant molecules at a desired growth temperature. This means that changes experienced by the surface of the nongrowth area must be one of the main reasons for loss of selectivity in AS-ALD. Hence, a fundamental understanding of microscopic growth phenomena is critical to further expanding the AS-ALD process to other systems requiring topographically selective coating in various emerging nanostructures.

In the present study, we investigate in depth the growth mechanisms of Pt ALD on the hydrophobic CF_x surface using a combination of experimental and theoretical methods. First, the growth characteristics of Pt ALD on the CF_x layer and thermal stability of the CF_x layer itself are experimentally investigated within a growth temperature window up to 350 °C. On the basis of density functional theory (DFT) calculations, we determine the reaction energies for adsorption of oxygen and the Pt precursor and for the formation of volatile reaction products generated during CF_x degradation. Finally, we propose that the overall reaction mechanism for Pt ALD on the CF_x layer is composed of O_2 adsorption, CF_x elimination, and eventual adsorption of the Pt precursor on CF_x-degraded regions of the substrate, allowing Pt nucleation. The main features of the proposed reaction mechanisms during Pt ALD on the CF_x-implanted surface are schematically illustrated in Figure 1.

■ EXPERIMENTAL AND THEORETICAL METHODS

ALD Processes. A custom-made ALD reactor controlled by LabVIEW software was used for Pt ALD. The ALD setup is designed to transport the precursors and carrier gas efficiently from the manifold to the substrate before it is exhausted through the pump. ALD of Pt films was carried out using $MeCpPtMe_3$ (trimethyl-

(methylcyclopentadienyl)platinum(IV), Sigma-Aldrich) and oxygen as the Pt precursor and counter reactant, respectively, across the temperature window of 225−350 °C. The Pt precursor contained in a glass bubbler was heated to 50 °C to obtain sufficient vapor pressure, and the delivery lines were heated to a temperature of 10−15 °C higher than that of the bubblers to prevent precursor condensation. The precursor vapor was carried into the reaction chamber with N_2 carrier gas controlled by a mass flow controller. N_2 gas at the same flow rate was also used for purging excess gas molecules and byproducts between each precursor and counter reactant exposure step. Further information on the Pt ALD process can be found in our earlier publications.[9,22]

Substrate Preparation Methods. The CF_x implantation process was performed on Si(001) blanket wafers at 1 kV with an implant dose of 1×10^{16} ions/cm^2 using a plasma implantation system with CF_4 gas (Applied Materials, Inc.), which led to the formation of an ultrathin CF_x-containing hydrophobic layer on the Si substrate. Contact angle images of water droplets show a difference in hydrophobicity before and after the formation of the CF_x layer.[9] The estimated water contact angle (WCA) values were 38.5° and 104.8°, respectively. For reference controls for a routine Pt ALD process, the Si(001) substrate was immersed in piranha solution (volume ratio, 3:1 of H_2SO_4/H_2O_2 mixture), leading to high surface hydrophilicity because of chemical oxide formation with an increased number of surface hydroxyl groups.[22−24]

Analytical Methods. The elemental composition and chemical bonding structure of the films were analyzed by X-ray photoelectron spectroscopy (XPS, PHI VersaProbe) using an Al $K\alpha$ monochromatic source of 1486.6 eV. The surface hydrophobicity was estimated from the WCA at three different spots using a contact angle goniometer (SL 100, Solon Tech.), and the average value was taken to represent the hydrophobicity of each film. In the contact angle measurement, the acute angle (0−90°) and obtuse angle (90−180°) signify a hydrophilic and hydrophobic nature of the surface layer, respectively.

The film thickness was measured by spectroscopic ellipsometry with a spectral range of 380−900 nm at three different angles of incidence (65, 70, and 75°) and with the polarizer set to 45°. The surface morphology of the films was analyzed by plan-view observation of scanning electron microscopy (SEM, FEI Magellan 400 XHR) and by atomic force microscopy (AFM, Digital Instruments Multimode Nanoscope IIIa), and the surface coverage was computed using ImageJ software from the planar SEM images. The cross-sectional view of Pt films was explored by transmission electron microscopy (TEM, FEI Titan 80−300). The microstructure of the films was analyzed by grazing incidence X-ray diffraction
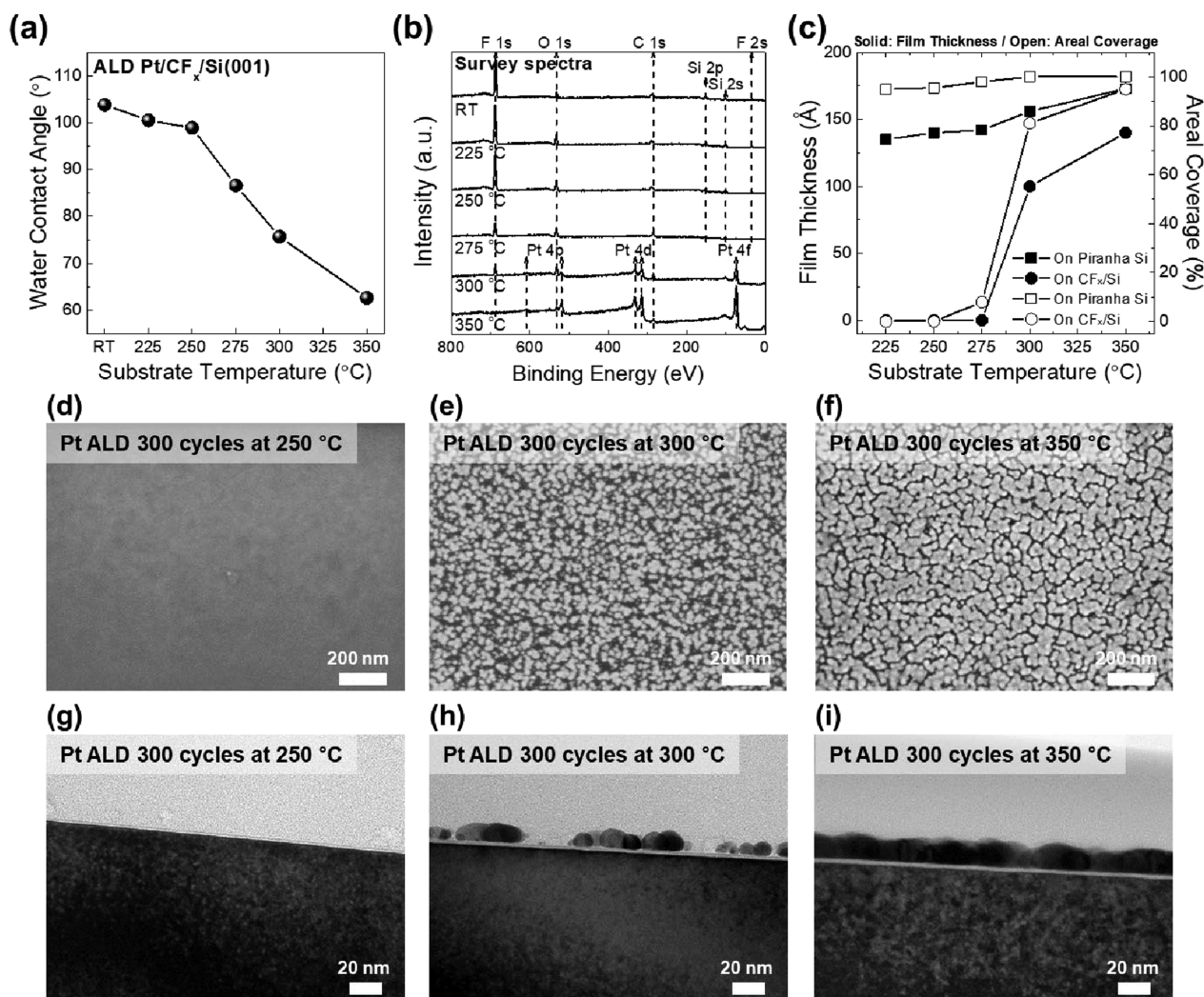
Figure 2. (a) WCA plotted as a function of substrate temperature, and (b) XPS survey scan spectra collected following 300 cycles of Pt ALD in a range of growth temperatures from 225 to 350 °C; the XPS spectrum of the bare CF_x layer is included for reference. (c) Film thickness (squares) and areal coverage (circles) plotted versus growth temperature for 300 cycles of Pt ALD on the CF_x layer and on the reference Si. (d–i) Plan-view SEM images and cross-sectional TEM images observed after 300 cycles of Pt ALD on the CF_x layer (d and g) at 250 °C, (e and h) at 300 °C, and (f and i) at 350 °C, respectively.

(GIXRD) performed at beam line 11–3 of the Stanford Synchrotron Radiation Lightsource. The GIXRD data were collected with a MAR345 2D imaging detector using a 12.7 KeV X-ray source with an incident angle of 0.5°. The detector was 150 mm away from the sample, and the position was calibrated using a LaB_6 reference and the WxDiff software package.

Computational Methods. DFT calculations were performed using the Quantum Espresso software package.[25] The generalized gradient approximation BEEF-vdw functional[26] was employed because of its ability to obtain an accurate description of molecular adsorption on solid surfaces and its consideration of van der Waals interaction. The core electrons were treated using the projector augmented wave methods.[27] The plane-wave cutoff used in all calculations was 400 eV and the density cutoff 4000 eV, and the k-point was sampled with a $2 \times 2 \times 1$ Monkhorst-pack grid. The convergence criteria for electronic and ionic relaxation were set to 10^{-5} eV and 0.05 eV/Å, respectively. A (2×2) supercell of the c(4 × 2)-Si(001) surface was used as the substrate, which has a thickness of eight atomic layers and has four buckled "dimers" on the surface (see Figure S2). The bottom four layers of the slab are fixed in their original bulk atomic positions, and the slabs are spaced with 20 Å of vacuum layers in between. As a model CF_x-covered surface, 1ML of CF_3 was adsorbed such that each Si atom of the surface dimer is

bonded to a CF_3 moiety. The adsorption energy can be calculated with eq 1, and the desorption energy is easily obtained with the reverse equation.

$$\Delta E_{ads} = \Delta E_{slab+mol} - (\Delta E_{slab} + \Delta E_{mol}) \tag{1}$$

Here, $\Delta E_{slab\ +\ mol}$ is the total energy of the system after adsorption, ΔE_{slab} is the energy of the surface, and ΔE_{mol} is the energy of the gas phase molecule.

The detailed binding site and the structure of CF_3-modified Si surfaces modeled as a function of coverage are shown in Figure S3. The Gibbs free energy was calculated to consider the effect of temperature using the following equation.[28]

$$\Delta G = \Delta E + \Delta ZPE - T\Delta S \tag{2}$$

Here, ΔE is the DFT energy change, ΔZPE is the zero-point energy change, ΔS is the entropy change, and T is the temperature. ΔS for gas phase molecules is taken from the thermodynamic table,[29,30] while ΔZPE and ΔS for the adsorbate are calculated as shown below.[28]

$$\Delta ZPE = \frac{1}{2} \sum_{i}^{DOF} h\upsilon_i \tag{3}$$

$$\Delta S = k_{\mathrm{B}} \sum_{\mathrm{i}}^{\mathrm{DOF}} \left[\frac{\varepsilon_{\mathrm{i}}}{k_{\mathrm{B}}T(e^{\varepsilon_{\mathrm{i}}/k_{\mathrm{B}}T} - 1)} - \ln(1 - e^{\varepsilon_{\mathrm{i}}/k_{\mathrm{B}}T}) \right] \quad (4)$$

Here, ε_{i} is $h\upsilon_{\mathrm{i}}$, and υ_{i} is the frequency from the DFT calculation.

■ RESULTS AND DISCUSSION

Pt ALD Processes on the CF$_x$ Surface. To understand the change in surface properties that occurs at the CF$_x$-modified substrate as a result of Pt ALD, WCA, XPS, and SEM measurements were carried out as a function of Pt ALD temperature. Figure 2(a) shows the change in the WCA following 300 cycles of Pt ALD at growth temperatures ranging from 225 to 350 °C, with that of the room temperature (RT) CF$_x$ layer also shown as a reference. With increasing growth temperature up to 350 °C, a significant decrease in the contact angle from ca. 105 to ca. 63° (see WCA images shown in Figure S4) was observed, indicative of the major influence of growth temperature. The WCA data for Pt ALD with very few incubation cycles on piranha-cleaned Si are available in Figure S5. The large decrease in the WCA suggests a degradation of the CF$_x$ layer with increasing temperature.

We anticipate that as the CF$_x$ layer degrades during the Pt ALD process, Pt nucleation and growth may begin to occur. To confirm the degradation of the CF$_x$ layer and the presence of corresponding Pt moieties, XPS survey scans were obtained, as shown in Figure 2(b), and the quantitative results of atomic compositions are summarized in Table 1. Consistent with the

Table 1. Summary of XPS Compositional Results Following 300 Cycles of Pt ALD in a Range of Growth Temperatures from 225 to 350°C[a]

| compositional analyses	F (at %)	O (at %)	C (at %)	Si (at %)	Pt (at %)
as-implanted CF$_x$ surface	51.6	14.0	22.2	12.2	
Pt ALD at 225 °C for 300 cycles	50.6	14.7	22.4	12.3	
Pt ALD at 250 °C for 300 cycles	49.0	15.4	21.9	13.7	
Pt ALD at 275 °C for 300 cycles	27.5	21.5	27.2	13.6	0.1
Pt ALD at 300 °C for 300 cycles	16.0	19.5	36.9	19.1	8.5
Pt ALD at 350 °C for 300 cycles		12.1	40.3		47.6

[a]Herein, the atomic composition of as-implanted CF$_x$ is shown as a reference.

WCA results, the XPS data indicated a noticeable decrease in the F 1s peak associated with a C−F covalent bond with increasing Pt ALD temperature. At the highest temperatures studied, there was also an increase in Pt peaks (Pt 4p, 4d, and 4f), which reveals that Pt growth is occurring on the CF$_x$-modified surface; namely, although no Pt signal was detected for temperatures up to 250 °C, a very small Pt signal (∼0.1 at. %) appeared at 275 °C, and a significant amount of Pt was observed above 300 °C. The correlation between the loss of the F signal and the rise of the Pt signal suggests that the onset of Pt nucleation is related to the degradation of C−F bonds.

The areal coverage of Pt extracted from plan-view SEM images (Figure 2(d−f)) and the film thickness determined from spectroscopic ellipsometry, benchmarked against cross-sectional TEM data (Figure 2(g,h)), are plotted versus the substrate temperature in Figure 2(c) for both CF$_x$-implanted Si

and reference piranha-cleaned Si substrates. The surface morphology and roughness are additionally measured by AFM (Figure S6). Nearly ∼100% Pt coverage was observed on the reference Si surface following 300 ALD cycles, regardless of the growth temperature. On the contrary, the areal coverage for Pt grown on the CF$_x$ layer remained very low for temperatures below 300 °C and then significantly increased to ∼95% at 350 °C. Very similar behavior was observed for the film thickness. GIXRD data collected after 300 cycles of Pt ALD on CF$_x$-implanted Si at temperatures from 225 to 350 °C are available in Figure S7.

Because these Pt ALD studies on the CF$_x$-covered substrate revealed that the Pt growth characteristics were sharply affected by the substrate temperature during ALD, we investigated the thermal stability of the CF$_x$ layer in the absence of ALD to provide insight into the origin of the CF$_x$ degradation mechanism. Figure 3(a) shows the WCA plots of
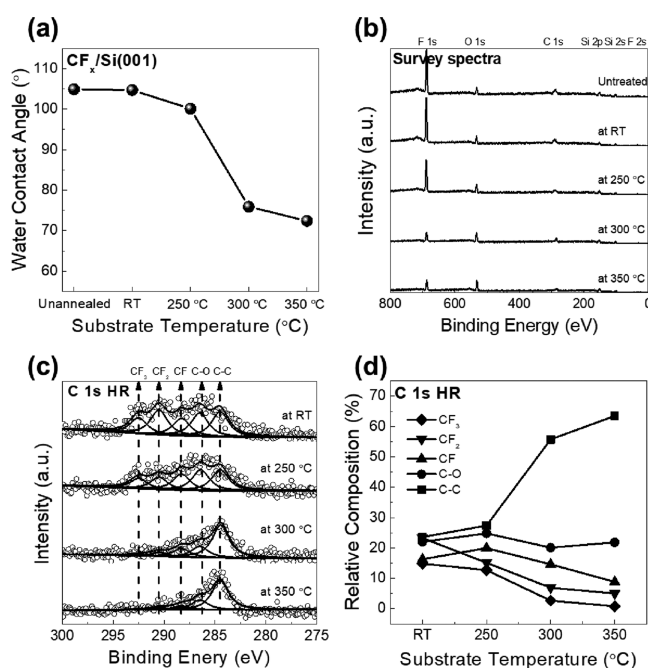
Figure 3. (a) WCA plotted and (b) XPS survey scan spectra collected after 2 h of vacuum annealing in the presence of O$_2$ (1.5 torr) in the ALD reactor over a range of temperatures from RT to 350 °C; data from a bare CF$_x$ layer are added as reference. (c) C 1s high-resolution XPS spectra collected after 2 h of vacuum annealing in the ALD reactor in a range of growth temperatures from RT to 350 °C. (d) Relative composition plots of CF$_3$, CF$_2$, CF, C−O, and C−C groups extracted from the C 1s high-resolution XPS spectra.

the CF$_x$-implanted substrate after 2 h of vacuum annealing in the same ALD reactor at temperatures ranging from RT to 350 °C; the unannealed CF$_x$-implanted substrate is also added as a reference. During the vacuum annealing, O$_2$ was flowed with a partial pressure of 1.5 torr into the reactor, identical to the condition for the oxygen exposure step during the Pt ALD. Consistent with the WCA results shown in Figure 2(a), we observed a significant reduction of the WCA from ca. 105 to ca. 72° (see WCA images shown in Figure S8). In particular, a notable drop in the WCA slope was found in between 250 and 300 °C, similar to the behavior observed after ALD at these temperatures (Figure 2(a)). XPS survey scans of the vacuum-annealed CF$_x$-implanted surfaces additionally revealed a

significant reduction in the fluorine-to-carbon (F/C) ratio (Figure 3(b)), with quantitative information about atomic compositions summarized in Table 2. To further elucidate

Table 2. Summary of XPS Compositional Results after Vacuum Annealing in the Presence of O$_2$ (1.5 Torr) for 2 h, where the Atomic Compositions of Unannealed CF$_x$ is Available as a Reference

| compositional analyses	F (at %)	O (at %)	C (at %)	Si (at %)	Pt (at %)
unannealed CF$_x$ surface	52.9	11.3	24.2	11.6	2.2
RT for 2 h	52.4	12.2	24.4	11.0	2.1
250 °C for 2 h	46.6	16.8	23.5	13.2	2.0
300 °C for 2 h	25.0	27.0	28.4	19.7	0.9
350 °C for 2 h	22.0	30.7	26.3	21.0	0.8

changes in the fluorocarbon (CF$_x$) bonding features, high-resolution spectra of the C 1s peak were collected as a function of annealing temperature. The C 1s spectrum is deconvoluted into five distinct peaks, which are assigned to CF$_3$ (292.5 eV), CF$_2$ (290.5 eV), CF (288.3 eV), C−O (286.5 eV), and C−C (284.5 eV) components, respectively, as shown in Figure 3(c). These peaks have good correspondence with reference values in the literature for CF$_x$ films.[9,31−33] The effect of the substrate temperature on the relative concentrations of the different CF$_x$ moieties is clearly evident in Figure 3(c). Relative compositions of the different carbon species extracted from the high-resolution XPS spectra are plotted in Figure 3(d). The data show that not only there a significant increase in the concentration of nonfluorinated C−C moieties with increasing annealing temperature, but also there is a corresponding reduction in the concentration of CF groups. Such carbon residues are likely to retard growth of Pt, although perhaps not as well as the CF$_x$ groups as shown in Figure 2(c). In short, it is evident that the CF groups are thermally labile, eventually allowing formation of volatile products. Further information on changes in WCA and XPS data after the vacuum annealing without oxygen exposure up to 5 h is available in Figure S9.

DFT Calculations for Pt ALD Reactions on the CF$_x$ Surface. In previous literature, the reaction mechanism during Pt ALD was understood as cyclic repetition of the following: during the O$_2$ half-cycle, the surface-adsorbed carbonaceous layer is removed by catalytic combustion, and an oxidized surface layer forms; in the other half-cycle composed of the MeCpPtMe$_3$ pulse, hydrocarbon ligands decompose on the surface by reacting with the surface oxygen atoms until the surface oxygen is depleted, at which point they leave a carbonaceous layer on the surface.[34,35] To elucidate the fundamental aspects of Pt ALD on the CF$_x$-modified surfaces, we performed DFT calculations examining two aspects of the process: the first studied the binding properties of the Pt precursor at the Si substrate with and without the CF$_x$ layer, and the second investigated the thermal elimination of the CF$_x$ layer.

Because the substrate is repeatedly exposed to O$_2$ at elevated temperatures through the Pt ALD process, it can be expected that the surface becomes oxidized regardless of deposition of Pt.[36] The binding energies of O on the Si(001) slab and on the CF$_x$ covered Si(001) are −5.28 and − 5.39 eV, respectively, values much stronger than that on most transition metals,[37] and there is a clear linear relation between transition state energy (O$_2$ dissociation energy) and product energy (2O

energy) according to the Brønsted−Evans−Polanyi relation,[38,39] which means that the surface of Si(001) will be saturated with dissociated O atoms. Therefore, our calculations examining the outcome of O$_2$ exposure focused on the bonding configuration of oxygen atoms on clean and CF$_x$-covered Si, with the results shown in Figure S10. It was found that O located on top of the CF$_x$ layer is unstable, but O can strongly bind to the topmost Si atoms regardless of the presence of the CF$_x$ layer. In fact, the adsorption energies of O at the CF$_x$ covered Si surface are nearly identical to those on the bare Si surface (Figure S10). Therefore, it can be assumed that initial partial oxidation of the substrate will occur at the underlying Si layer, and moreover all the possible binding sites will be fully occupied with O atoms upon repeated O$_2$ gas injection during the Pt ALD process. This oxidized Si(001) substrate beneath the CF$_x$ layer is therefore used in our subsequent calculations of the Pt ALD mechanism.

A comparative analysis of the molecular and dissociative adsorption energetics of the MeCpPtMe$_3$ precursor on O-adsorbed Si versus CF$_x$/O-adsorbed Si is shown in Figure 4.
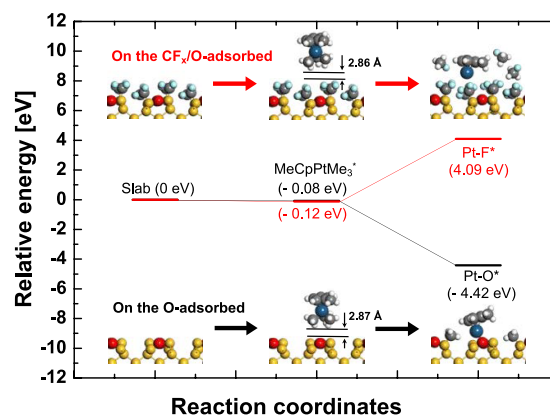

Figure 4. Relative energy diagram of the MeCpPtMe$_3$ precursor decomposition process on the O-adsorbed surface (black) and on the CF$_x$/O-adsorbed surface (red).

We assumed a simple decomposition process for the MeCpPtMe$_3$ precursor, which allows us to achieve a basic intuition and to compare across the two surfaces, even though the actual decomposition could be much more complicated. For dissociative adsorption in the Pt precursor exposure step, we studied dissociation of the MeCpPtMe$_3$ precursor into methyl groups (Me$_3$) and a Pt atom bound to the cyclopentadienyl ring (MeCpPt). Both the methyl groups and the Pt atom in MeCpPt can bind to the Si(001) surface after dissociation. On both surfaces, the energetics before the Pt precursor dissociatively adsorbs is the same; that is, there is no significant difference between O-adsorbed and CF$_x$/O-adsorbed surfaces. However, significant energy changes are calculated upon dissociative adsorption of the Pt precursor. First, on the O-adsorbed Si(001) surface, the Pt precursor decomposes into a PtMeCp group directly bonded to surface O and methyl groups bonded to Si atoms, with a reaction exoenergicity of −4.42 eV (black). In contrast, on the CF$_x$/O-adsorbed surface, the most stable product calculated was generation of gaseous CH$_3$F molecules and PtMeCp bound to surface C atoms; however, with an endoenergicity of 4.09 eV (red), this product was unstable. Importantly, because of the large size of the Pt precursor, it is difficult for it to penetrate

through the CF_x layer to form a bond with a surface-bound O atom. Therefore, the presence of the CF_x layer can block deposition of Pt.

We also calculated the temperature dependence of the thermodynamics of desorption of the CF_x layer. The change in Gibbs free energy (ΔG) can be approximated using eq 2. All the parameters were obtained from DFT calculations[28] and standard tables for gas-phase molecules (see Table S2).[29,30] We considered three possible species generated from the CF_x-terminated surface, F_2, CF_3, and CF_4, and we compared the desorption energy of each species at $T = -273$ °C and 300 °C. As shown in Figure 5 with the black lines, formation of all
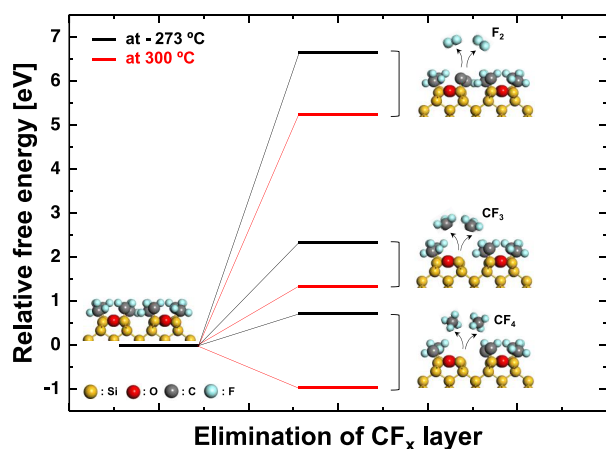
Figure 5. Gibbs free energy diagram of the loss of F_2, CF_3, and CF_4 species from the CF_x/O-adsorbed Si surface at different temperatures: -273 °C (black) and 300 °C (red).

three species is unfavorable at -273 °C (F_2 at 6.64 eV, CF_3 at 2.33 eV, and CF_4 at 0.72 eV). However, at a higher temperature of 300 °C (red lines), desorption of CF_4 becomes spontaneous -0.97 eV ($\Delta G < 0$), while production of F_2 (ca. 5.25 eV) or CF_3 (ca. 1.34 eV) remains energetically unfavorable. The energies of these two products are too unstable to be overcome by entropy at 300 °C. The size of the energy change caused by entropy at 300 °C is on the order of 1.0 eV for all of the products; that is, they are not much different from each other. These results suggest that production of gas-phase CF_4, enabled by entropic factors, may lead to the experimentally observed temperature dependence. At lower temperatures, the CF_x-terminated surface is stable, but at higher temperatures, evolution of CF_4 can occur. Therefore, removal of the CF_x layer is enabled at elevated temperatures through desorption of CF_4, and eventually Pt nucleation and growth will begin to occur from the degraded CF_x region. Both these steps are consistent with the experimental observations of loss of F and uptake of Pt at the surface at elevated temperatures.

CONCLUSIONS

CF_x modification of surfaces has been used in AS-ALD to control Pt deposition. We investigated the growth characteristics of Pt ALD on the hydrophobic CF_x surface at growth temperatures ranging from 225 to 350 °C. We confirmed the blocking efficacy of the CF_x layer against Pt ALD at temperatures below 300 °C; in contrast, the CF_x layer was unable to inhibit Pt ALD at temperatures above 300 °C. Through thermal stability evaluation of the CF_x layer via WCA

and XPS analyses, a sharp sensitivity to the ALD temperature was observed, showing a significant loss in the thermally labile fluorine-rich CF_x groups at temperatures above 300 °C. On the basis of DFT calculations of surface reaction energetics of O_2 and $MeCpPtMe_3$ adsorption during each half-cycle of Pt ALD, the chemisorption of small O_2 molecules beneath the CF_x layer was shown to be facile, whereas chemisorption of the bulky $MeCpPtMe_3$ was prohibitive on the CF_x-modified surface. Furthermore, the DFT calculations for volatile products of thermal decomposition of the CF_x layer indicated that formation of CF_4 would become spontaneous at or above 300 °C. As a result, current study suggests an overall reaction mechanism during the Pt ALD process at temperatures above 300 °C in which the CF_x layer undergoes O_2 chemisorption and CF_4 elimination followed by $MeCpPtMe_3$ chemisorption onto the missing CF_x region, finally leading to Pt formation. The present work provides fundamental understanding of microscopic growth phenomena and thereby expands opportunities for topographically selective functional coatings onto various emerging nanostructures.

ASSOCIATED CONTENT

Supporting Information

The Supporting Information is available free of charge at https://pubs.acs.org/doi/10.1021/acs.chemmater.0c03372.

Additional characterization data for the WCA and AFM and DFT calculations (PDF)

AUTHOR INFORMATION

Corresponding Author

Stacey F. Bent — *Department of Chemical Engineering, Stanford University, Stanford, California 94305, United States;* orcid.org/0000-0002-1084-5336; Email: sbent@stanford.edu

Authors

Woo-Hee Kim — *Department of Chemical Engineering, Stanford University, Stanford, California 94305, United States; Department of Materials Science and Chemical Engineering, Hanyang University, Ansan 15588, Korea;* orcid.org/0000-0003-0868-7479

Kihyun Shin — *SUNCAT Center of Interface Science and Catalysis, SLAC National Accelerator Laboratory, Menlo Park, California 94025, United States; Department of Chemistry and Oden Institute of Computational Engineering and Sciences, University of Texas at Austin, Austin, Texas 78712, United States*

Bonggeun Shong — *Department of Chemical Engineering, Hongik University, Seoul 04066, Republic of Korea;* orcid.org/0000-0002-5782-6300

Ludovic Godet — *Applied Materials, Sunnyvale, California 94085, United States*

Complete contact information is available at:
https://pubs.acs.org/10.1021/acs.chemmater.0c03372

■ REFERENCES

(1) Lee, H.-B.-R.; Baeck, S. H.; Jaramillo, T. F.; Bent, S. F. Growth of Pt Nanowires by Atomic Layer Deposition on Highly Ordered Pyrolytic Graphite. *Nano Lett.* **2013**, *13*, 457−463.

(2) Xie, J.; Yang, X.; Han, B.; Shao-Horn, Y.; Wang, D. Site-Selective Deposition of Twinned Platinum Nanoparticles on TiSi$_2$ Nanonets by Atomic Layer Deposition and Their Oxygen Reduction Activities. *ACS Nano* **2013**, *7*, 6337−6345.

(3) Cheng, N.; Banis, M. N.; Liu, J.; Riese, A.; Li, X.; Li, R.; Ye, S.; Knights, S.; Sun, X. Extremely Stable Platinum Nanoparticles Encapsulated in a Zirconia Nanocage by Area-Selective Atomic Layer Deposition for the Oxygen Reduction Reaction. *Adv. Mater.* **2015**, *27*, 277−281.

(4) Singh, J. A.; Thissen, N. F. W.; Kim, W.-H.; Johnson, H.; Kessels, W. M. M.; Bol, A. A.; Bent, S. F.; Mackus, A. J. M. Area-Selective Atomic Layer Deposition of Metal Oxides on Noble Metals through Catalytic Oxygen Activation. *Chem. Mater.* **2018**, *30*, 663−670.

(5) Kim, K.; Lee, H.-B.-R.; Johnson, R. W.; Tanskanen, J. T.; Liu, N.; Kim, M.-G.; Pang, C.; Ahn, C.; Bent, S. F.; Bao, Z. Selective metal deposition at graphene line defects by atomic layer deposition. *Nat. Commun.* **2014**, *5*, 4781.

(6) Li, R.; Zhang, F.; Wang, D.; Yang, J.; Li, M.; Zhu, J.; Zhou, X.; Han, H.; Li, C. Spatial separation of photogenerated electrons and holes among {010} and {110} crystal facets of BiVO$_4$. *Nat. Commun.* **2013**, *4*, 1432.

(7) Stevens, E.; Tomczak, Y.; Chan, B. T.; Altamirano Sanchez, E.; Parsons, G. N.; Delabie, A. Area-Selective Atomic Layer Deposition of TiN, TiO$_2$, and HfO$_2$ on Silicon Nitride with inhibition on Amorphous Carbon. *Chem. Mater.* **2018**, *30*, 3223−3232.

(8) Mameli, A.; Merkx, M. J. M.; Karasulu, B.; Roozeboom, F.; Kessels, W. M. M.; Mackus, A. J. M. Area-Selective Atomic Layer Deposition of SiO$_2$ Using Acetylacetone as a Chemoselective Inhibitor in an ABC-Type Cycle. *ACS Nano* **2017**, *11*, 9303−9311.

(9) Kim, W.-H.; Minaye Hashemi, F. S.; Mackus, A. J. M.; Singh, J.; Kim, Y.; Bobb-Semple, D.; Fan, Y.; Kaufman-Osborn, T.; Godet, L.; Bent, S. F. A Process for Topographically Selective Deposition on 3D Nanostructures by Ion Implantation. *ACS Nano* **2016**, *10*, 4451−4458.

(10) Chen, R.; Bent, S. F. Chemistry for Positive Pattern Transfer Using Area-Selective Atomic Layer Deposition. *Adv. Mater.* **2006**, *18*, 1086−1090.

(11) Seo, S.; Yeo, B. C.; Han, S. S.; Yoon, C. M.; Yang, J. Y.; Yoon, J.; Yoo, C.; Kim, H.-j.; Lee, Y.-b.; Lee, S. J.; Myoung, J.-M.; Lee, H.-B.-R.; Kim, W.-H.; Oh, I.-K.; Kim, H. Reaction Mechanism of Area-Selective Atomic Layer Deposition for Al$_2$O$_3$ Nanopatterns. *ACS Appl. Mater. Interfaces* **2017**, *9*, 41607−41617.

(12) Liddle, J. A.; Gallatin, G. M. Nanomanufacturing: A Perspective. *ACS Nano* **2016**, *10*, 2995−3014.

(13) Lee, J. P.; Sung, M. M. A New Patterning Method Using Photocatalytic Lithography and Selective Atomic Layer Deposition. *J. Am. Chem. Soc.* **2004**, *126*, 28−29.

(14) Park, M. H.; Jang, Y. J.; Sung-Suh, H. M.; Sung, M. M. Selective Atomic Layer Deposition of Titanium Oxide on Patterned Self-Assembled Monolayers Formed by Microcontact Printing. *Langmuir* **2004**, *20*, 2257−2260.

(15) Kobayashi, N. P.; Donley, C. L.; Wang, S.-Y.; Williams, R. S. Atomic layer deposition of aluminum oxide on hydrophobic and hydrophilic surfaces. *J. Cryst. Growth* **2007**, *299*, 218−222.

(16) Ras, R. H. A.; Sahramo, E.; Malm, J.; Raula, J.; Karppinen, M. Blocking the Lateral Film Growth at the Nanoscale in Area-Selective Atomic Layer Deposition. *J. Am. Chem. Soc.* **2008**, *130*, 11252−11253.

(17) Huang, J.; Lee, M.; Lucero, A.; Cheng, L.; Kim, J. Area-Selective ALD of TiO$_2$ Nanolines with Electron-Beam Lithography. *J. Phys. Chem. C* **2014**, *118*, 23306−23312.

(18) Minaye Hashemi, F. S.; Prasittichai, C.; Bent, S. F. Self-Correcting Process for High Quality Patterning by Atomic Layer Deposition. *ACS Nano* **2015**, *9*, 8710−8717.

(19) Chopra, S. N.; Zhang, Z.; Kaihlanen, C.; Ekerdt, J. G. Selective Growth of Titanium Nitride on HfO$_2$ across Nanolines and Nanopillars. *Chem. Mater.* **2016**, *28*, 4928−4934.

(20) Hashemi, F. S. M.; Bent, S. F. Sequential Regeneration of Self-Assembled Monolayers for Highly Selective Atomic Layer Deposition. *Adv. Mater. Interfaces* **2016**, *3*, 1600464.

(21) Parsons, G. N. Functional model for analysis of ALD nucleation and quantification of area-selective deposition. *Journal of Vacuum Science & Technology A* **2019**, *37*, No. 020911.

(22) Lee, H.-B.-R.; Bent, S. F. Microstructure-Dependent Nucleation in Atomic Layer Deposition of Pt on TiO$_2$. *Chem. Mater.* **2011**, *24*, 279−286.

(23) Klier, K.; Shen, J. H.; Zettlemoyer, A. C. Water on silica and silicate surfaces. I. Partially hydrophobic silicas. *J. Phys. Chem.* **1973**, *77*, 1458−1465.

(24) Morita, M.; Ohmi, T.; Hasegawa, E.; Kawakami, M.; Ohwada, M. Growth of native oxide on a silicon surface. *J. Appl. Phys.* **1990**, *68*, 1272−1281.

(25) Paolo, G.; Stefano, B.; Nicola, B.; Matteo, C.; Roberto, C.; Carlo, C.; Davide, C.; Guido, L. C.; Matteo, C.; Ismaila, D.; Andrea Dal, C.; Stefano de, G.; Stefano, F.; Guido, F.; Ralph, G.; Uwe, G.; Christos, G.; Anton, K.; Michele, L.; Layla, M.-S.; Nicola, M.; Francesco, M.; Riccardo, M.; Stefano, P.; Alfredo, P.; Lorenzo, P.; Carlo, S.; Sandro, S.; Gabriele, S.; Ari, P. S.; Alexander, S.; Paolo, U.; Renata, M. W. QUANTUM ESPRESSO: a modular and open-source software project for quantum simulations of materials. *J. Phys.: Condens. Matter* **2009**, *21*, 395502.

(26) Wellendorff, J.; Lundgaard, K. T.; Møgelhøj, A.; Petzold, V.; Landis, D. D.; Nørskov, J. K.; Bligaard, T.; Jacobsen, K. W. Density functionals for surface science: Exchange-correlation model development with Bayesian error estimation. *Phys. Rev. B* **2012**, *85*, 235149.

(27) Kresse, G.; Joubert, D. From ultrasoft pseudopotentials to the projector augmented-wave method. *Phys. Rev. B* **1999**, *59*, 1758−1775.

(28) Howalt, J. G.; Bligaard, T.; Rossmeisl, J.; Vegge, T. DFT based study of transition metal nano-clusters for electrochemical NH$_3$ production. *Phys. Chem. Chem. Phys.* **2013**, *15*, 7785−7795.

(29) Weast, R. C., *CRC Handbook of Chemistry and Physics*. 49th ed.; The Chemical Ruber Company: Cleveland, OH 1968.

(30) Atkins, P. W., *Physical Chemistry*. 6th ed.; Oxford Univeristy Press: Oxford, U.K., 1998.

(31) Oehrlein, G. S.; Zhang, Y.; Vender, D.; Haverlag, M. Fluorocarbon high-density plasmas. I. Fluorocarbon film deposition and etching using CF$_4$ and CHF$_3$. *J. Vac. Sci. & Technol. A* **1994**, *12*, 323−332.

(32) Pehrsson, P. E.; Zhao, W.; Baldwin, J. W.; Song, C.; Liu, J.; Kooi, S.; Zheng, B. Thermal Fluorination and Annealing of Single-Wall Carbon Nanotubes. *J. Phys. Chem. B* **2003**, *107*, 5690−5695.

(33) Le, Q. T.; de Marneffe, J.-F.; Conard, T.; Vaesen, I.; Struyf, H.; Vereecke, G. Effect of UV Irradiation on Modification and Subsequent Wet Removal of Model and Post-Etch Fluorocarbon Residues. *J. Electrochem. Soc.* **2012**, *159*, H208−H213.

(34) Mackus, A. J. M.; Leick, N.; Baker, L.; Kessels, W. M. M. Catalytic Combustion and Dehydrogenation Reactions during Atomic Layer Deposition of Platinum. *Chem. Mater.* **2012**, *24*, 1752−1761.

(35) Geyer, S. M.; Methaapanon, R.; Shong, B.; Pianetta, P. A.; Bent, S. F. In Vacuo Photoemission Studies of Platinum Atomic Layer Deposition Using Synchrotron Radiation. *J. Phys. Chem. Lett.* **2012**, *4*, 176−179.

(36) Massoud, H. Z. The onset of the thermal oxidation of silicon from room temperature to 1000°C. *Microelectron. Eng.* **1995**, *28*, 109−116.

(37) Nørskov, J. K.; Rossmeisl, J.; Logadottir, A.; Lindqvist, L.; Kitchin, J. R.; Bligaard, T.; Jónsson, H. Origin of the Overpotential for Oxygen Reduction at a Fuel-Cell Cathode. *J. Phys. Chem. B* **2004**, *108*, 17886−17892.

(38) Bligaard, T.; Nørskov, J. K.; Dahl, S.; Matthiesen, J.; Christensen, C. H.; Sehested, J. The Brønsted−Evans−Polanyi relation and the volcano curve in heterogeneous catalysis. *J. Catal.* **2004**, *224*, 206−217.

(39) Cheng, J.; Hu, P.; Ellis, P.; French, S.; Kelly, G.; Lok, C. M. Brønsted−Evans−Polanyi Relation of Multistep Reactions and Volcano Curve in Heterogeneous Catalysis. *J. Phys. Chem. C* **2008**, *112*, 1308−1311.